



*Supplement of*

**Measurement report: The variation properties of aerosol hygroscopic growth related to chemical composition during new particle formation days in a coastal city of Southeast China**

**Lingjun Li et al.**

*Correspondence to:* Mengren Li ([mrli@iue.ac.cn](mailto:mrli@iue.ac.cn)) and Jinsheng Chen ([jschen@iue.ac.cn](mailto:jschen@iue.ac.cn))

The copyright of individual parts of the supplement might differ from the article licence.

**Table S1.** The hygroscopicity parameters ( $\kappa$ ) and densities ( $\rho$ ) of inorganic salts used in this study.

| Species                      | NH <sub>4</sub> NO <sub>3</sub> | (NH <sub>4</sub> ) <sub>2</sub> SO <sub>4</sub> | NH <sub>4</sub> HSO <sub>4</sub> | NH <sub>4</sub> Cl |
|------------------------------|---------------------------------|---|----------------------------------|--------------------|
| $\kappa$                     | 0.58                            | 0.48  | 0.56                             | 0.93               |
| $\rho$ (g cm <sup>-3</sup> ) | 1.72                            | 1.769   | 1.78                             | 1.527              |

**Table S2.** Comparisons of the average  $f(80\%)$ ,  $f(85\%)$  and  $f(70\%)$  values in different study.

| Study area            | Periods               | $f(\text{RH})$  | RH(%) | Reference               |
|-----------------------|-----------------------|-----------------|-------|-------------------------|
| Lin'an, China         | 2013/3/1-31           | $1.43 \pm 0.12$ | 80    | Zhang et al.<br>(2015)  |
|                       |                       | $1.58 \pm 0.12$ | 85    |                         |
| Raoyang, China        | 2014/6/17 - 8/16      | $2.28 \pm 0.69$ | 80    | Wu et al.<br>(2017)     |
|                       |                       | $3.39 \pm 1.14$ | 85    |                         |
| Beijing, China        | 2017/1/12 – 2/14      | $1.47 \pm 0.16$ | 80    | Zhao et al.<br>(2019)   |
| Beijing, China        | 2019/9/19 - 10/4      | $1.64 \pm 0.13$ | 85    | Ren et al.<br>(2021)    |
| Guangzhou, China      | 2019/10/15 - 2020/1/8 | $1.50 \pm 0.11$ | 70    | Li et al. (2021)        |
| Ny- Ålesund, Svalbard | 2008/7/15 – 10/13     | $3.24 \pm 0.63$ | 85    | Zieger et al.<br>(2010) |
| Jungfrauoch, Swiss    | 2008/5                | $2.30 \pm 0.33$ | 85    | Zieger et al.<br>(2013) |
| Mace Head, Ireland    | 2009/1-2              | $2.08 \pm 0.29$ | 85    |                         |
| Granada, Spain        | 2013/4/4 – 5/10       | $1.60 \pm 0.30$ | 85    | Titos et al.<br>(2014)  |
| Xiamen, China         | 2022/2 - 4            | $1.44 \pm 0.15$ | 80    | This study              |
|                       |                       | $1.60 \pm 0.16$ | 85    |                         |

**Table S3.** Statistical analysis of particle concentration distribution ( $\text{cm}^{-3}$ ) for different days from February to April 2022.

|                   |        | NPF                | Undefined          | Non-NPF            | Entire campaign    |
|-------------------|--------|--------------------|--------------------|--------------------|--------------------|
| Total             | mean   | $6.31 \times 10^3$ | $5.72 \times 10^3$ | $3.41 \times 10^3$ | $5.29 \times 10^3$ |
|                   | stdv   | $3.60 \times 10^3$ | $2.61 \times 10^3$ | $1.91 \times 10^3$ | $2.82 \times 10^3$ |
|                   | max    | $1.67 \times 10^4$ | $3.05 \times 10^4$ | $1.15 \times 10^4$ | $3.05 \times 10^4$ |
|                   | median | $5.60 \times 10^3$ | $5.37 \times 10^3$ | $2.82 \times 10^3$ | $4.91 \times 10^3$ |
|                   | min    | $1.08 \times 10^3$ | $6.57 \times 10^2$ | $5.50 \times 10^2$ | $5.50 \times 10^2$ |
| Nucleation mode   | mean   | $1.66 \times 10^3$ | $1.15 \times 10^3$ | $6.99 \times 10^2$ | $1.12 \times 10^3$ |
|                   | stdv   | $1.59 \times 10^3$ | $8.25 \times 10^2$ | $5.16 \times 10^2$ | $9.52 \times 10^2$ |
|                   | max    | $8.34 \times 10^3$ | $8.57 \times 10^3$ | $5.28 \times 10^3$ | $8.57 \times 10^3$ |
|                   | median | $1.06 \times 10^3$ | $9.40 \times 10^2$ | $5.81 \times 10^2$ | $8.64 \times 10^2$ |
|                   | min    | $1.05 \times 10^2$ | $6.59 \times 10$   | $2.00 \times 10$   | $2.00 \times 10$   |
| Aitken mode       | mean   | $3.80 \times 10^3$ | $3.37 \times 10^3$ | $1.78 \times 10^3$ | $3.08 \times 10^3$ |
|                   | stdv   | $2.80 \times 10^3$ | $1.82 \times 10^3$ | $1.08 \times 10^3$ | $1.98 \times 10^3$ |
|                   | max    | $1.44 \times 10^4$ | $2.21 \times 10^4$ | $6.09 \times 10^3$ | $2.21 \times 10^4$ |
|                   | median | $2.97 \times 10^3$ | $3.10 \times 10^3$ | $1.43 \times 10^3$ | $2.73 \times 10^3$ |
|                   | min    | $5.47 \times 10^2$ | $3.02 \times 10^2$ | $2.60 \times 10^2$ | $2.60 \times 10^2$ |
| Accumulation mode | mean   | $8.59 \times 10^2$ | $1.20 \times 10^3$ | $9.33 \times 10^2$ | $1.10 \times 10^3$ |
|                   | stdv   | $4.04 \times 10^2$ | $6.12 \times 10^2$ | $6.20 \times 10^2$ | $6.08 \times 10^2$ |
|                   | max    | $2.42 \times 10^3$ | $7.67 \times 10^3$ | $4.99 \times 10^3$ | $7.67 \times 10^3$ |
|                   | median | $7.82 \times 10^2$ | $1.11 \times 10^3$ | $7.55 \times 10^2$ | $1.01 \times 10^3$ |
|                   | min    | $2.09 \times 10^2$ | $3.73 \times 10$   | $8.75 \times 10$   | $3.73 \times 10$   |

**Table S4.** The curve-fitting parameters for  $f(\text{RH})$  for different aerosol types using Eq.(1).

|                  |                      | $a$   | $b$   | Reference             |
|------------------|----------------------|-------|-------|-----------------------|
| Entire campaign  | RH < 60%             | 1.02  | 0.21  | Chen et al.<br>(2014) |
|                  | RH $\geq$ 60%        | 1.08  | 0.26  |                       |
| Clean            | RH < 60%             | 1.00  | 0.10  |                       |
|                  | RH $\geq$ 60%        | 1.00  | 0.26  |                       |
| Polluted         | RH < 60%             | 1.03  | 0.26  |                       |
|                  | RH $\geq$ 60%        | 1.14  | 0.25  |                       |
| Very clean       |                      | 0.930 | 0.329 | Zhao et al.<br>(2019) |
| Moderately clean | 12 Jan.-14 Feb. 2017 | 0.971 | 0.372 |                       |
| Polluted         |                      | 0.988 | 0.356 |                       |
| Very clean       |                      | 0.972 | 0.355 |                       |
| Moderately clean | 6 July-21 Aug. 2017  | 0.980 | 0.362 |                       |
| Polluted         |                      | 0.984 | 0.371 |                       |
| Very clean       |                      | 0.979 | 0.334 |                       |
| Moderately clean | 30 Sep.-13 Nov. 2017 | 1.002 | 0.344 |                       |
| Polluted         |                      | 1.014 | 0.332 |                       |
| NPF              | Feb.-Apr. 2022       | 0.993 | 0.257 | This work             |
| Non-NPF          |                      | 1.026 | 0.289 |                       |

**Table S5.** Statistics on the mass concentration ( $\mu\text{g m}^{-3}$ ) of aerosol species (S.D.: standard deviation)

|          | Mean | S.D. | Maximum | Minimum |
|----------|------|------|---------|---------|
| Sulfate  | 1.82 | 1.08 | 6.54    | 0.02    |
| Nitrate  | 2.75 | 3.28 | 24.46   | 0.03    |
| Ammonium | 1.26 | 1.04 | 6.26    | 0.02    |
| Chlorine | 0.16 | 0.17 | 1.89    | 0.001   |
| OM       | 4.84 | 3.85 | 52.22   | 0.18    |
| BC       | 0.95 | 0.62 | 3.51    | 0.10    |

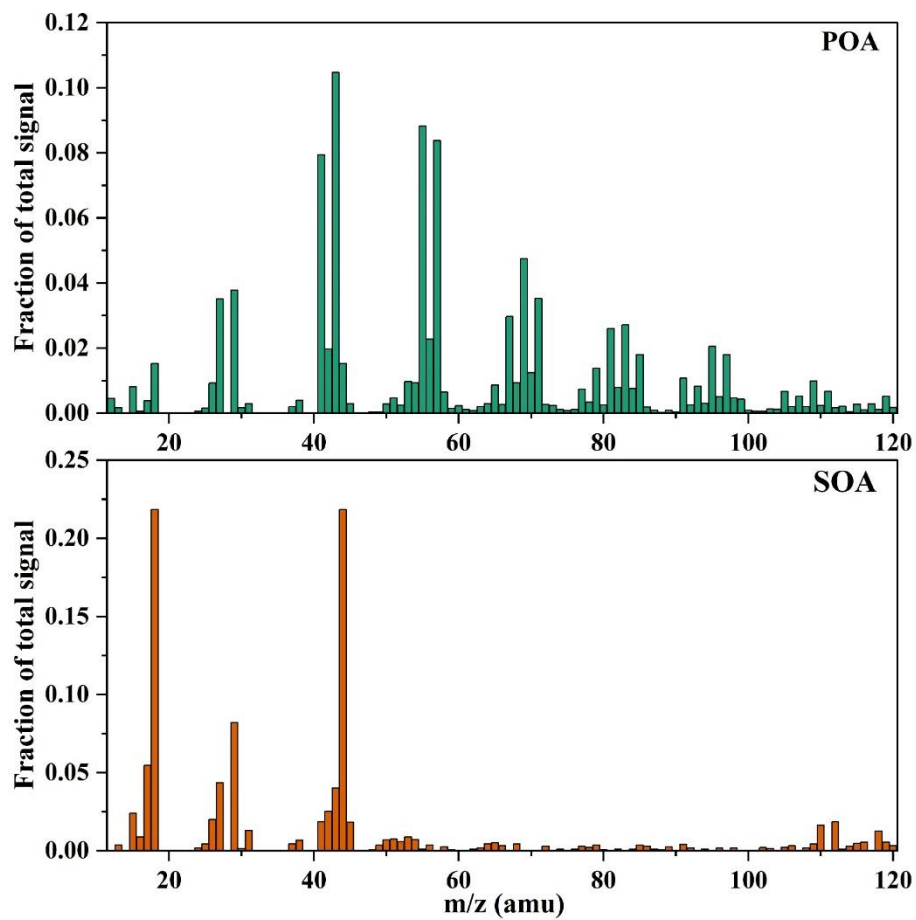
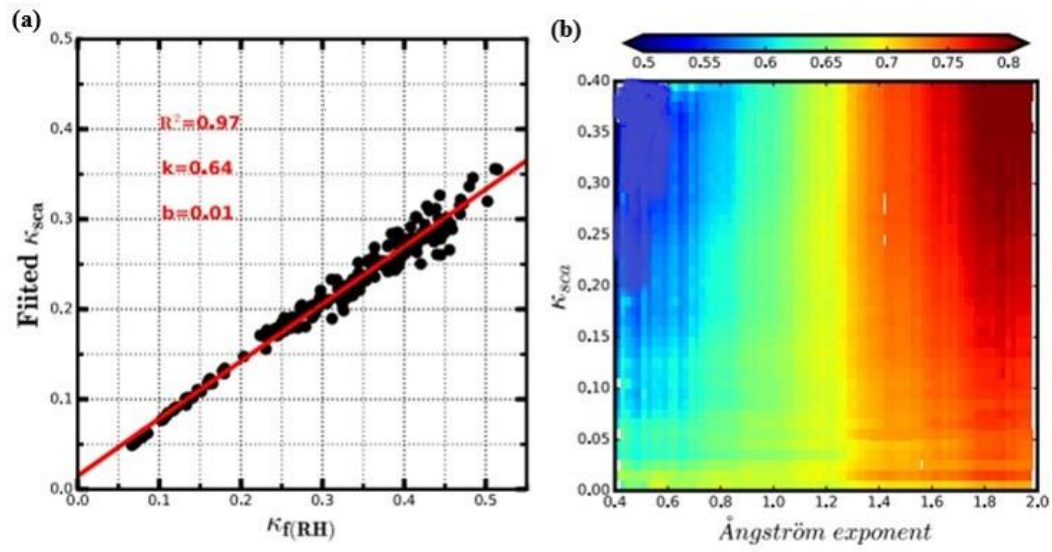
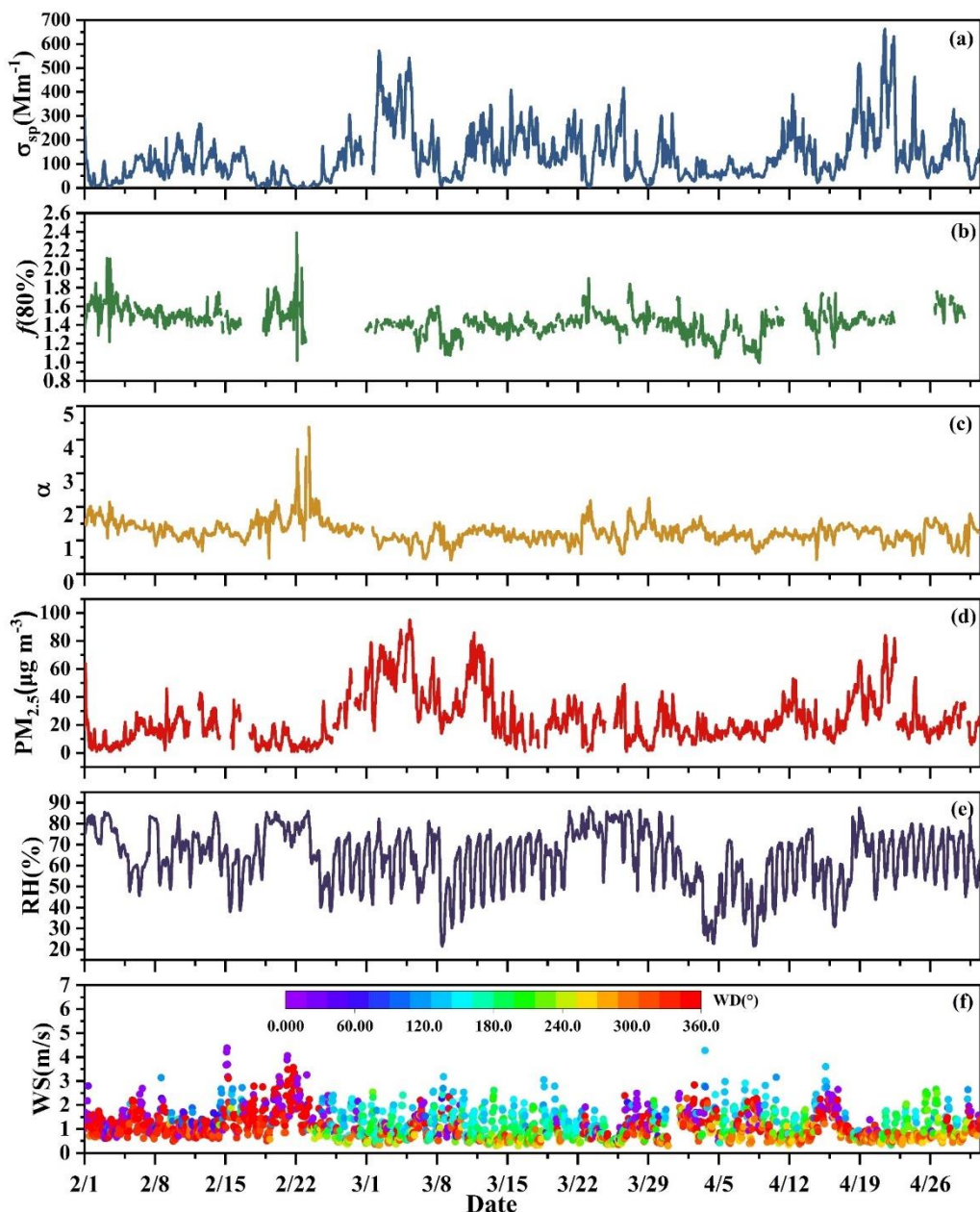


Figure S1. Mass spectra of two OA factors.



**Figure S2.** The calculation method of  $\kappa_{f(RH)}$  (Kuang et al., 2017). (a) The good linear relationship between  $\kappa_{f(RH)}$  and  $\kappa_{sca}$ . (b) Colors represent  $R_\kappa$  values and the color bar is shown at the top of this figure. The x axis represents the Ångström exponent and the y axis represents  $\kappa_{sca}$ .



**Figure S3. Time series of measured and derived aerosol variables and ambient RH, wind speed and direction from February to April 2022.** (a) Aerosol scattering coefficient of DryNeph at 525 nm wavelength; (b) the aerosol scattering hygroscopic growth factor  $f(80\%)$  at 525 nm wavelength; (c) scattering Ångström exponents  $\alpha$ ; (d)  $PM_{2.5}$  mass concentrations; (e) relative humidity (RH) at ambient conditions; (f) wind speed (WS) and wind direction (WD).

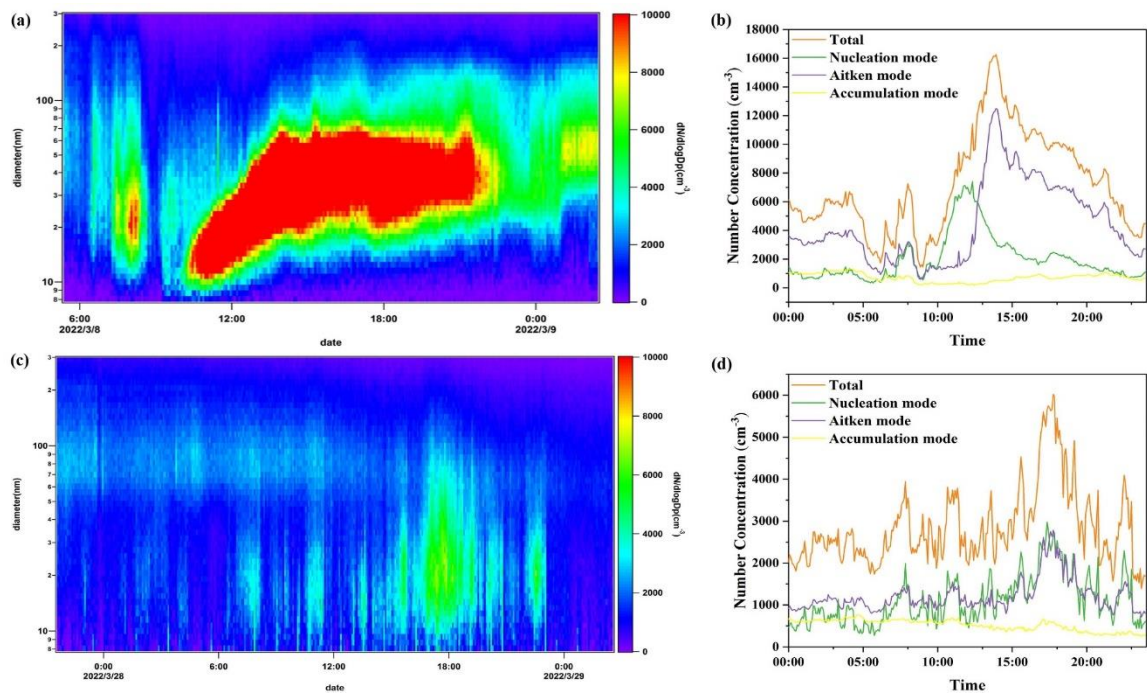


**Figure S4. the particle number size distribution spectrum and number concentration. Example of NPF (a, b) and Non-NPF (c, d) days.**

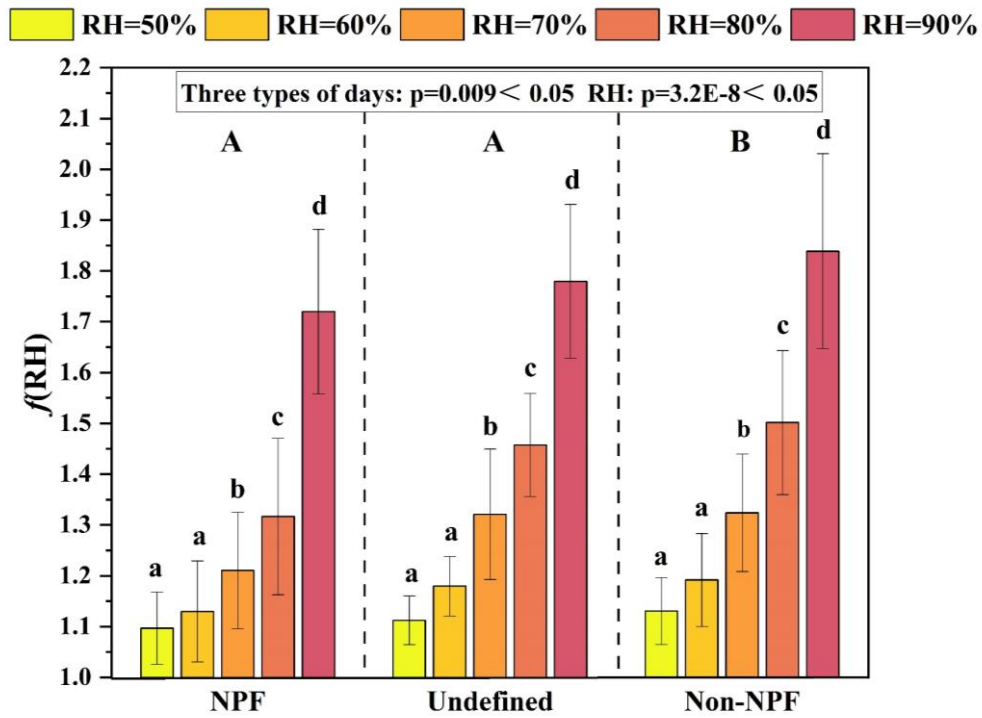


**Figure S5. Effects of different days and RH on  $f(\text{RH})$ .** Different capital letters (A, B) indicate significant differences among three types of days as determined by ANOVA with posthoc comparisons ( $p < 0.05$ ). Different lowercase letters (a, b, c and d) indicate significant differences among different RH levels as determined by ANOVA with posthoc comparisons ( $p < 0.05$ ). Data are represented as mean  $\pm$  SD ( $n=2$ ).

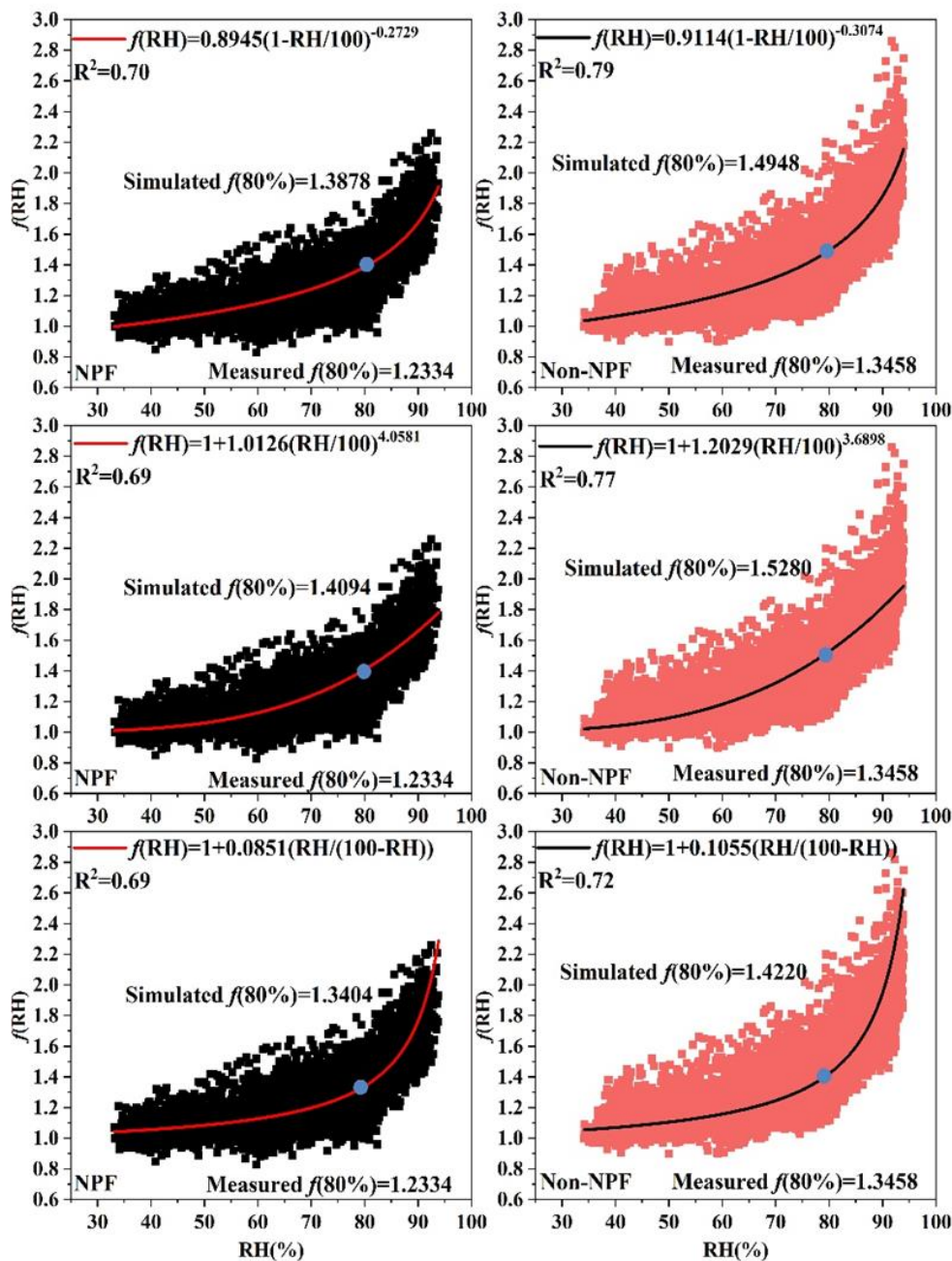
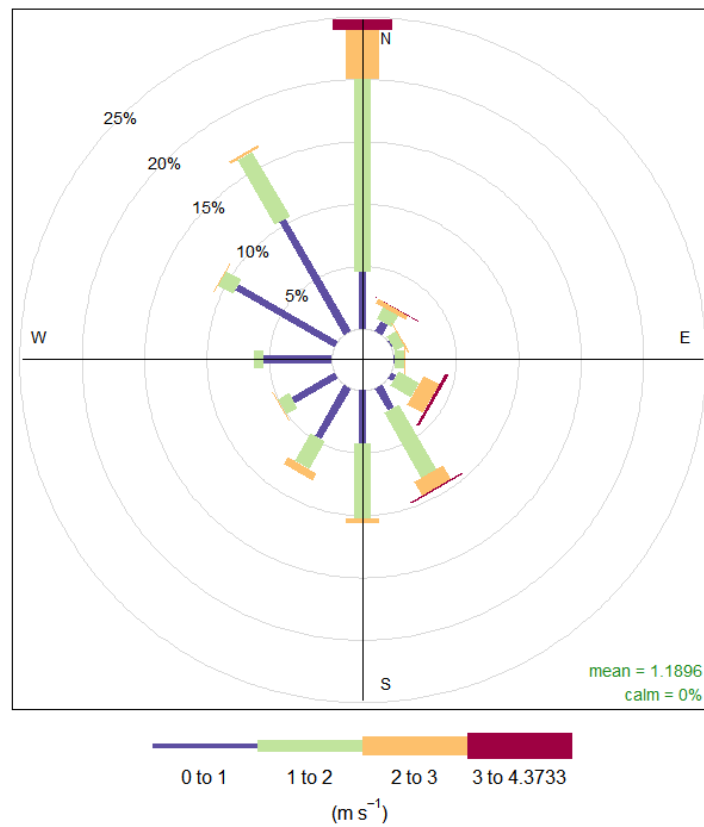


**Figure S6. Comparisons of the  $f(\text{RH})$  fitted curves following the other three parameterization schemes on NPF and Non-NPF events.** Black: NPF, red: Non-NPF. The first row shows the results fitted by Eq. (S6), the second row shows the results fitted by Eq. (S7), and the third row shows the results fitted by Eq. (S8).



**Frequency of counts by wind direction (%)**

**Figure S7. The wind directions and speeds at observation site during the observation period.**

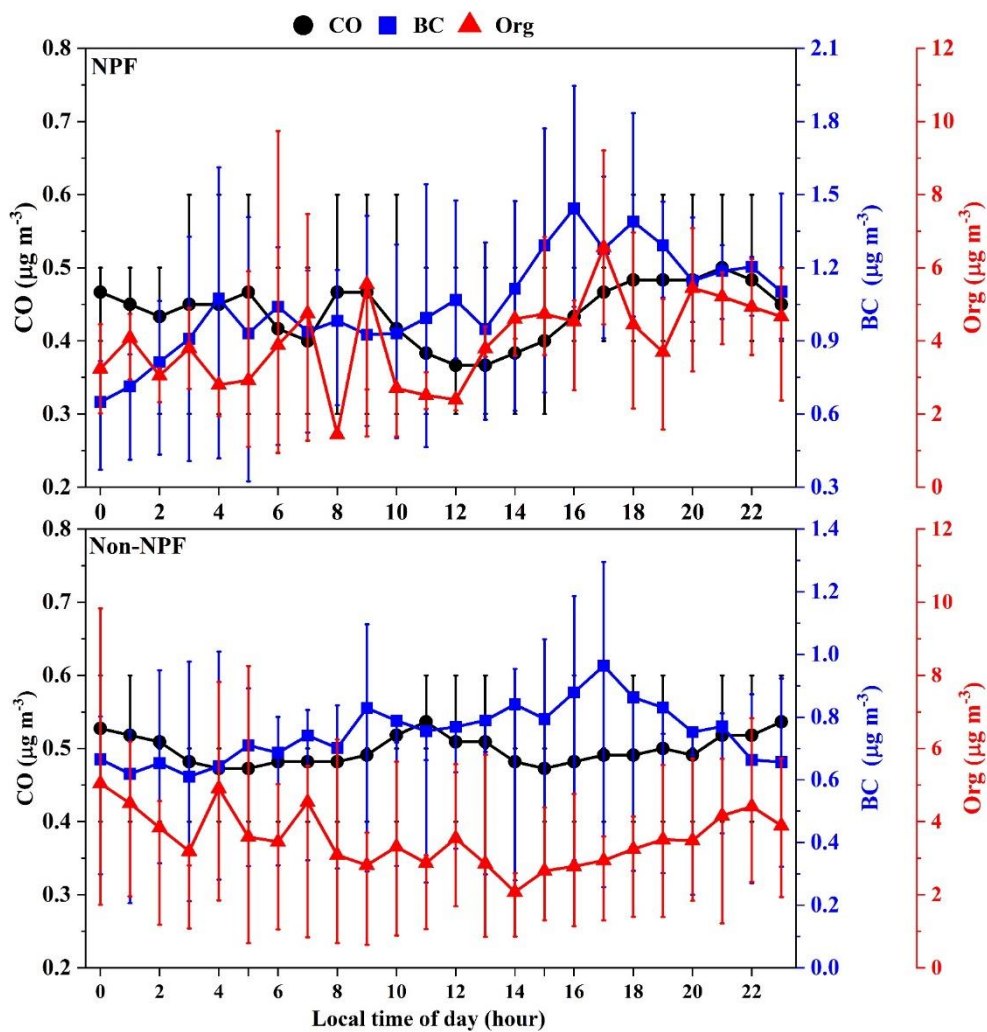


**Figure S8. Diurnal variations of CO, BC and Org on NPF (a) and non-NPF (b) days.**

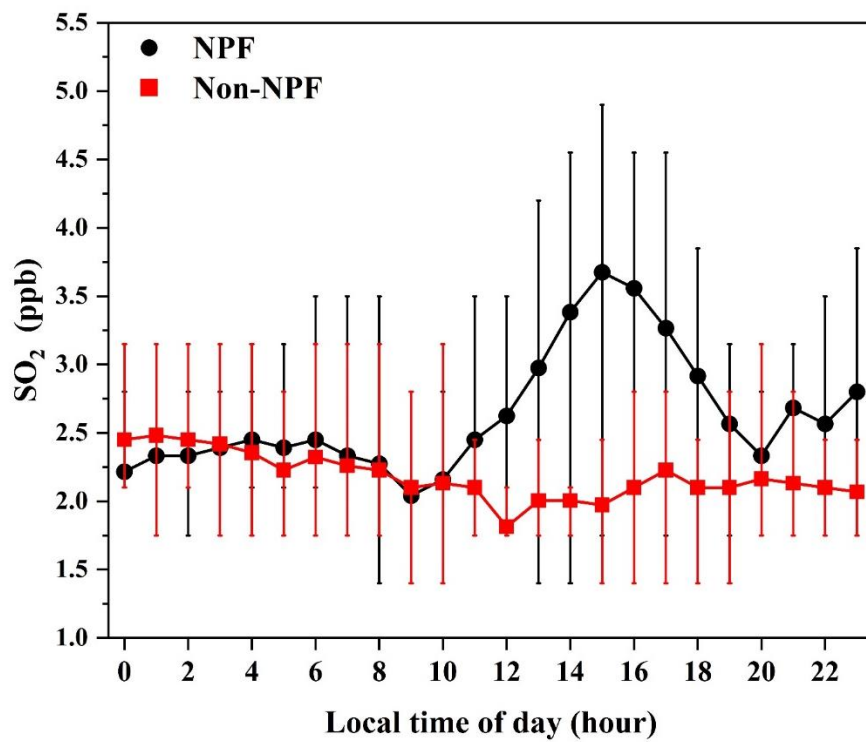
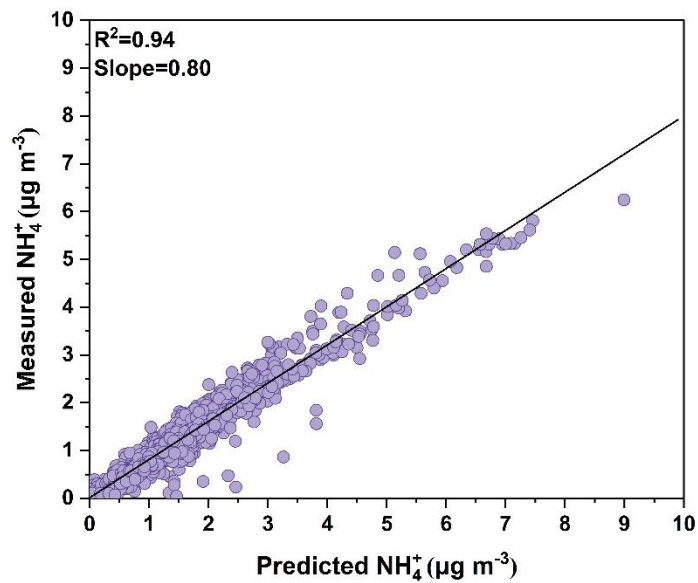
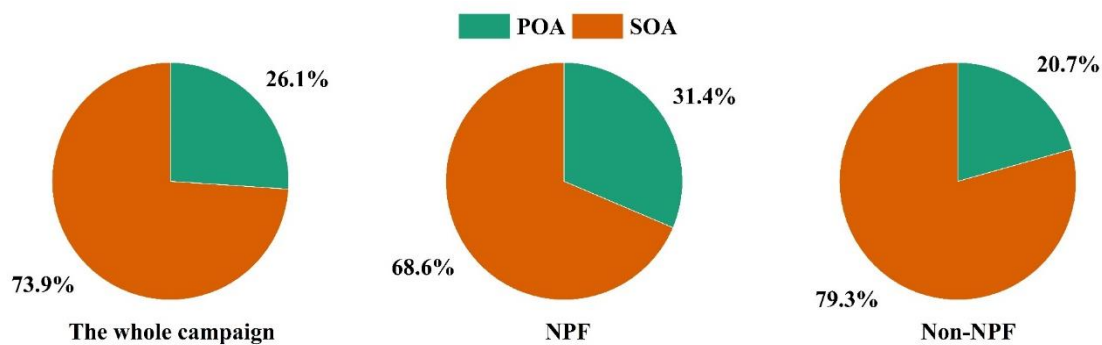


Figure S9. Diurnal variations of SO<sub>2</sub> on NPF and non-NPF days.



**Figure S10. Measured and predicted mass concentration of ammonium.** The predicted mass concentration of ammonium (predicted  $\text{NH}_4^+$ ) is calculated by Eq. (S9). The solid line represents the linear regression.



**Figure S11. The proportions of POA and SOA in OA.**

## Section S1.

The multi-band dual-nephelometer system consisted of a nephelometer for aerosol scattering coefficients under dry conditions and another nephelometer for humidified aerosols. The sample airflow initially entered and passed through Nafion dryers which could reduce the RH of the airflow below 30%. After this, the airflow was divided into two routes, one was directed straight into the nephelometer; while the other was humidified via a Gore-Tex tube set in a stainless steel tube before flowing into the other nephelometer. The space between these two tubes contained circulating water. The temperature cycle of the circulating water layer was controlled by two water baths, which provided circulating water alternatively for the humidifier. When one water bath was heating up the water for humidifying, the RH of the airflow through the humidifier increased as the water temperature rose. Simultaneously, another water bath was cooling down the water itself, and no water entered the humidifier. When the airflow had been humidified to a setting maximum RH, the water bath with cool water was switched into the humidifier, causing the RH of the airflow to drop rapidly. As the water bath was heated, the RH of the airflow then rose gradually again. The temperature of the water in the water baths was controlled by an automatic system to ensure the humidifying effect. In addition, a control software system was used to make sure the RH scans were within a certain RH range. Two combined RH and temperature sensors (Vaisala HMP110; accuracy of  $\pm 0.2^\circ$  and  $\pm 1.7\%$  for RH ranges from 0 to 90 %, respectively, and accuracy of  $\pm 2.5\%$  for RH ranges from 90 to 100 % according to the manufacturer) were placed at the inlet and outlet of the nephelometer for humidified aerosols, and the measured RHs and temperatures were defined as  $RH_1/T_1$  and  $RH_2/T_2$ , respectively. The dew points at the inlet and outlet of the nephelometer for humidified aerosols were calculated using the measured  $RH_1/T_1$  and  $RH_2/T_2$ , and the average value was considered as the dew point of the sample air. The sample RH can be calculated through the derived dew point and the sample temperature, which is measured by the sensor inside the sample cavity of the nephelometer (Liu and Zhao, 2016; Kuang et al., 2017; Zhao et al., 2019). The system was adjusted and calibrated before the enhanced observations. During the campaign, the two nephelometers were cleaned and calibrated every 2 weeks.

## Section S2.

The ACSM data were analyzed using the standard Wave Metrics Igor Pro data analysis software (version 6.37). PMF was applied using the Igor Pro-based PMF Evaluation Toolkit (PET) to identify OA factors by analyzing high-time-resolution mass spectra (Paatero and Tapper, 1994; Ulbrich et al., 2009). We constrained the POA using SoFi (version 6.G) along with the multi-linear engine (ME-2) algorithm (Canonaco et al., 2013). In this study, only values of  $m/z < 120$  were used, as the fraction of signals with  $m/z > 120$  was minor in total signals and associated with larger uncertainties (Sun et al., 2012; Chen et al., 2022). The large uncertainty for  $m/z > 120$  was likely due to low ion transmission efficiency and significant interferences from naphthalene signals on some  $m/z$ 's (e.g.,  $m/z$  127, 128, and 129). Ions with a signal-to-noise ratio (SNR)  $< 0.2$  were removed, and those with a SNR of 0.2–2 were down-weighted by a factor of 2. We used the spectral profiles of POA derived from standard spectra as constraints to analyze the source of organic matrices throughout the entire observation period (Ng et al., 2011). No other factors were constrained. After distinguishing the mass spectrum, analyzing the diurnal variation of the factors, and comparing the time series of the factors and external tracers, the PMF/ME-2 analysis of OA mass spectra resolved two OA factors: POA and SOA (Figure S1).

### Section S3.

Brock et al. (2016) proposed a single-parameter representation equation for describing  $f(\text{RH})$ . The equation for  $f(\text{RH})$  is written as:

$$f(\text{RH}) = 1 + \kappa_{\text{sca}} \frac{\text{RH}}{100 - \text{RH}} \quad (\text{S1})$$

Where,  $\kappa_{\text{sca}}$  is a parameter that fits  $f(\text{RH})$  best.

During processes of measuring  $f(\text{RH})$  with the multi-band dual-nephelometer system, the sample RH in the dry nephelometer condition ( $\text{RH}_0$ ) is not zero. Based on Eq. (S1), the measured  $f(\text{RH})_{\text{measured}}$  should be fitted using the following equation (Kuang et al., 2017):

$$f(\text{RH})_{\text{measured}} = \frac{1 + \kappa_{\text{sca}} \frac{\text{RH}}{100 - \text{RH}}}{1 + \kappa_{\text{sca}} \frac{\text{RH}_0}{100 - \text{RH}_0}} \quad (\text{S2})$$

According to (Kuang et al., 2017), there is a good linear relationship between  $\kappa_{f(\text{RH})}$  and  $\kappa_{\text{sca}}$  (Figure S2a). The ratio  $\kappa_{\text{sca}} / \kappa_{f(\text{RH})}$  ( $R_{\kappa}$ ) can be estimated by a look-up table based on the Ångström exponent and  $\kappa_{\text{sca}}$  (Figure S2b). With this look-up table,  $R_{\kappa}$  and  $\kappa_{f(\text{RH})}$  can be directly obtained from measurements of the multi-band dual-nephelometer system. A software for deriving the aerosol hygroscopicity parameter based on measurements from the multi-band dual-nephelometer system and the above principles (BMET, China) was used to obtain  $\kappa_{f(\text{RH})}$  in this study.

#### Section S4.

The  $\kappa_{chem}$  of this study can be calculated by the following equation (Petters and Kreidenweis, 2007):

$$\kappa_{chem} = \sum_i \kappa_i \cdot \varepsilon_i \quad (S3)$$

where  $\kappa_i$  and  $\varepsilon_i$  denote the hygroscopicity parameter  $\kappa$  and the volume fraction of chemical component  $i$  in the aerosol. Based on Eq.(S6) and Supplementary Table S5,  $\kappa_{chem}$  can be expressed as follows:

$$\kappa_{chem} = \kappa_{AN}\varepsilon_{AN} + \kappa_{AS}\varepsilon_{AS} + \kappa_{ABS}\varepsilon_{ABS} + \kappa_{AC}\varepsilon_{AC} + \kappa_{BC}\varepsilon_{BC} + \kappa_{OA}\varepsilon_{OA} \quad (S4)$$

Where,  $\kappa_{BC}$  is the  $\kappa$  of the black carbon aerosol (BC), which is assumed to be zero because BC is hydrophobic;  $\kappa_{OA}$  and  $\varepsilon_{OA}$  represent the  $\kappa$  and volume fraction of the total organic matter. The total aerosol volume concentration used to calculate the volume fraction was calculated by summing the volume concentrations of all chemical species (AN, AS, ABS, AC, BC and OA). The volume concentration of BC was calculated by assuming a density of  $1.7 \text{ g cm}^{-3}$ , and the volume concentration of OA was calculated by assuming that the density of POA is  $1 \text{ g cm}^{-3}$  and density of SOA is  $1.4 \text{ g cm}^{-3}$  (Wu et al., 2016).

## Section S5.

There are some characteristics of NPF and Non-NPF events (Figure S4). When NPF events occurred, the particle number size distribution showed an obvious “banana shape”, and the nucleation-mode particles exhibited a clear growth process for several hours. In Non-NPF days, the concentration of nucleation-mode particles did not exhibit a notable peak, and the growth process of particles did not appear. The onset time of NPF events observed in this study typically occurred around 10:00, coinciding with a sudden and rapid increase in the number concentration of nucleation-mode particles ( $N_{\text{nuc}}$ ). The diurnal variation of  $N_{\text{nuc}}$  exhibited a unimodal pattern, with the peak concentration occurring around 12:00. Following the increase in  $N_{\text{nuc}}$ , the number concentration of aitken-mode particles subsequently rose, reaching a peak concentration around 15:00, with a time delay of several hours after the peak of nucleation-mode particles, mainly caused by growth progress of particles from nucleation mode to a larger particle size range.

## Section S6.

The  $f(\text{RH})$  values were fitted with four frequently-used empirical equations. The comparison of the fitting results,  $R^2$  values, simulated and measured values of  $f(80\%)$  for each parameterization scheme reveals that Eq. (S5) had the best fitting curve, the highest  $R^2$  value, and it also had the smallest difference between simulated and measured values of  $f(80\%)$ . Therefore, Eq. (S5) was considered to be the most suitable parameterization scheme. The fitted curves of the other three parameterization schemes are shown in Figure S6.

$$f(\text{RH}) = a\left(1 - \frac{\text{RH}}{100}\right)^{-b\left(\frac{\text{RH}}{100}\right)} \quad (\text{S5})(\text{Chen et al., 2014})$$

$$f(\text{RH}) = a\left(1 - \frac{\text{RH}}{100}\right)^{-b} \quad (\text{S6})(\text{Kasten, 1969})$$

$$f(\text{RH}) = 1 + a\left(\frac{\text{RH}}{100}\right)^b \quad (\text{S7})(\text{Kotchenruther and Hobbs, 1998})$$

$$f(\text{RH}) = 1 + a\left(\frac{\text{RH}}{100 - \text{RH}}\right) \quad (\text{S8})(\text{Brock et al., 2016})$$

## Section S7.

Aerosol acidity is a crucial parameter affecting the aerosol hygroscopic growth. This is usually assessed by comparing the measured mass concentration of  $\text{NH}_4^+$  with the amount required to completely neutralize sulfate, nitrate, and chloride ions (predicted  $\text{NH}_4^+$ ), which can be obtained from the following equation (Sun et al., 2010):

$$\text{predicted } \text{NH}_4^+ = 18 \times \left( 2 \times \frac{\text{SO}_4^{2-}}{96} + \frac{\text{NO}_3^-}{62} + \frac{\text{Cl}^-}{35.5} \right) \quad (\text{S9})$$

The relationship between measured  $\text{NH}_4^+$  and predicted  $\text{NH}_4^+$  was demonstrated by Figure S10. The correlation between measured and predicted  $\text{NH}_4^+$  was very strong ( $r^2=0.94$ ), with a regression slope of 0.8, revealing that there were insufficient atmospheric  $\text{NH}_4^+$  to fully neutralise sulfate and nitrate, thereby,  $\text{PM}_1$  in Xiamen was considered to be more acidic during the observation period. Thus, the main chemical form of the sulfate aerosol was  $\text{NH}_4\text{HSO}_4$ , and the nitrate aerosol was in the form of  $\text{NH}_4\text{NO}_3$ . However, the average mass concentration of chloride ions was low in Xiamen during observation period, so the mass concentration of  $\text{NH}_4\text{Cl}$  was also low, with  $\text{NH}_4\text{NO}_3$ ,  $\text{NH}_4\text{HSO}_4$  and  $(\text{NH}_4)_2\text{SO}_4$  as the dominant inorganic components.

## Supplementary References

- Brock, C. A., Wagner, N. L., Anderson, B. E., Attwood, A. R., Beyersdorf, A., Campuzano-Jost, P., Carlton, A. G., Day, D. A., Diskin, G. S., Gordon, T. D., Jimenez, J. L., Lack, D. A., Liao, J., Markovic, M. Z., Middlebrook, A. M., Ng, N. L., Perring, A. E., Richardson, M. S., Schwarz, J. P., Washenfelder, R. A., Welti, A., Xu, L., Ziemba, L. D., and Murphy, D. M.: Aerosol optical properties in the southeastern United States in summer - Part 1: Hygroscopic growth, *Atmos. Chem. Phys.*, 16, 4987-5007, <http://doi.org/10.5194/acp-16-4987-2016>, 2016.
- Canonaco, F., Crippa, M., Slowik, J. G., Baltensperger, U., and Prévôt, A. S. H.: SoFi, an IGOR-based interface for the efficient use of the generalized multilinear engine (ME-2) for the source apportionment: ME-2 application to aerosol mass spectrometer data, *Atmos. Meas. Tech.*, 6, 3649-3661, <http://doi.org/10.5194/amt-6-3649-2013>, 2013.
- Chen, J., Zhao, C. S., Ma, N., and Yan, P.: Aerosol hygroscopicity parameter derived from the light scattering enhancement factor measurements in the North China Plain, *Atmos. Chem. Phys.*, 14, 8105-8118, <http://doi.org/10.5194/acp-14-8105-2014>, 2014.
- Chen, Y. P., Yang, C., Xu, L. L., Chen, J. S., Zhang, Y. R., Shi, J. Y., Fan, X. L., Zheng, R. H., Hong, Y. W., and Li, M. R.: Chemical composition of NR-PM1 in a coastal city of Southeast China: Temporal variations and formation pathways, *Atmos. Environ.*, 285, <http://doi.org/10.1016/j.atmosenv.2022.119243>, 2022.
- Kasten, F.: VISIBILITY FORECAST IN PHASE OF PRE-CONDENSATION, *Tellus*, 21, 630-&, <http://doi.org/10.1111/j.2153-3490.1969.tb00469.x>, 1969.
- Kotchenruther, R. A. and Hobbs, P. V.: Humidification factors of aerosols from biomass burning in Brazil, *J. Geophys. Res.:Atmos.*, 103, 32081-32089, <http://doi.org/10.1029/98jd00340>, 1998.
- Kuang, Y., Zhao, C. S., Tao, J. C., Bian, Y. X., Ma, N., and Zhao, G.: A novel method for deriving the aerosol hygroscopicity parameter based only on measurements from a humidified nephelometer system, *Atmos. Chem. Phys.*, 17, 6651-6662, <http://doi.org/10.5194/acp-17-6651-2017>, 2017.
- Li, J. W., Zhang, Z. S., Wu, Y. F., Tao, J., Xia, Y. J., Wang, C. Y., and Zhang, R. J.: Effects of chemical compositions in fine particles and their identified sources on hygroscopic growth factor during dry season in urban Guangzhou of South China, *Sci. Total Environ.*, 801, <http://doi.org/10.1016/j.scitotenv.2021.149749>, 2021.
- Liu, H. and Zhao, C.: Design of a Humidified Nephelometer System with High Time Resolution, *Acta Scientiarum Naturalium Universitatis Pekinensis*, 52, 999-1004, 2016.
- Ng, N. L., Herndon, S. C., Trimborn, A., Canagaratna, M. R., Croteau, P. L., Onasch, T. B., Sueper, D., Worsnop, D. R., Zhang, Q., Sun, Y. L., and Jayne, J. T.: An Aerosol Chemical Speciation Monitor (ACSM) for Routine Monitoring of the Composition and Mass Concentrations of Ambient Aerosol, *Aerosol Sci. Technol.*, 45, 780-794, <http://doi.org/10.1080/02786826.2011.560211>, 2011.
- Paatero, P. and Tapper, U.: POSITIVE MATRIX FACTORIZATION - A NONNEGATIVE FACTOR MODEL WITH OPTIMAL UTILIZATION OF ERROR-ESTIMATES OF DATA VALUES, *Environmetrics*, 5, 111-126,

<http://doi.org/10.1002/env.3170050203>, 1994.

Petters, M. D. and Kreidenweis, S. M.: A single parameter representation of hygroscopic growth and cloud condensation nucleus activity, *Atmos. Chem. Phys.*, 7, 1961-1971, <http://doi.org/10.5194/acp-7-1961-2007>, 2007.

Ren, R. M., Li, Z. Q., Yan, P., Wang, Y. Y., Wu, H., Cribb, M., Wang, W., Jin, X. A., Li, Y. A., and Zhang, D. M.: Measurement report: The effect of aerosol chemical composition on light scattering due to the hygroscopic swelling effect, *Atmos. Chem. Phys.*, 21, 9977-9994, <http://doi.org/10.5194/acp-21-9977-2021>, 2021.

Sun, J. Y., Zhang, Q., Canagaratna, M. R., Zhang, Y. M., Ng, N. L., Sun, Y. L., Jayne, J. T., Zhang, X. C., Zhang, X. Y., and Worsnop, D. R.: Highly time- and size-resolved characterization of submicron aerosol particles in Beijing using an Aerodyne Aerosol Mass Spectrometer, *Atmos. Environ.*, 44, 131-140, <http://doi.org/10.1016/j.atmosenv.2009.03.020>, 2010.

Sun, Y. L., Wang, Z. F., Dong, H. B., Yang, T., Li, J., Pan, X. L., Chen, P., and Jayne, J. T.: Characterization of summer organic and inorganic aerosols in Beijing, China with an Aerosol Chemical Speciation Monitor, *Atmos. Environ.*, 51, 250-259, <http://doi.org/10.1016/j.atmosenv.2012.01.013>, 2012.

Titos, G., Lyamani, H., Cazorla, A., Sorribas, M., Foyo-Moreno, I., Wiedensohler, A., and Alados-Arboledas, L.: Study of the relative humidity dependence of aerosol light-scattering in southern Spain, *Tellus B*, 66, <http://doi.org/10.3402/tellusb.v66.24536>, 2014.

Ulbrich, I. M., Canagaratna, M. R., Zhang, Q., Worsnop, D. R., and Jimenez, J. L.: Interpretation of organic components from Positive Matrix Factorization of aerosol mass spectrometric data, *Atmos. Chem. Phys.*, 9, 2891-2918, <http://doi.org/10.5194/acp-9-2891-2009>, 2009.

Wu, Y. F., Wang, X. J., Yan, P., Zhang, L. M., Tao, J., Liu, X. Y., Tian, P., Han, Z. W., and Zhang, R. J.: Investigation of hygroscopic growth effect on aerosol scattering coefficient at a rural site in the southern North China Plain, *Sci. Total Environ.*, 599, 76-84, <http://doi.org/10.1016/j.scitotenv.2017.04.194>, 2017.

Wu, Z. J., Zheng, J., Shang, D. J., Du, Z. F., Wu, Y. S., Zeng, L. M., Wiedensohler, A., and Hu, M.: Particle hygroscopicity and its link to chemical composition in the urban atmosphere of Beijing, China, during summertime, *Atmos. Chem. Phys.*, 16, 1123-1138, <http://doi.org/10.5194/acp-16-1123-2016>, 2016.

Zhang, L., Sun, J. Y., Shen, X. J., Zhang, Y. M., Che, H., Ma, Q. L., Zhang, Y. W., Zhang, X. Y., and Ogren, J. A.: Observations of relative humidity effects on aerosol light scattering in the Yangtze River Delta of China, *Atmos. Chem. Phys.*, 15, 8439-8454, <http://doi.org/10.5194/acp-15-8439-2015>, 2015.

Zhao, P. S., Ding, J., Du, X., and Su, J.: High time-resolution measurement of light scattering hygroscopic growth factor in Beijing: A novel method for high relative humidity conditions, *Atmos. Environ.*, 215, <http://doi.org/10.1016/j.atmosenv.2019.116912>, 2019.

Zieger, P., Fierz-Schmidhauser, R., Weingartner, E., and Baltensperger, U.: Effects of

relative humidity on aerosol light scattering: results from different European sites, *Atmos. Chem. Phys.*, 13, 10609-10631, <http://doi.org/10.5194/acp-13-10609-2013>, 2013.

Zieger, P., Fierz-Schmidhauser, R., Gysel, M., Strom, J., Henne, S., Yttri, K. E., Baltensperger, U., and Weingartner, E.: Effects of relative humidity on aerosol light scattering in the Arctic, *Atmos. Chem. Phys.*, 10, 3875-3890, <http://doi.org/10.5194/acp-10-3875-2010>, 2010.